*Article*

# Ultrasonic-Assisted Synthesis of 2D $\alpha$-Fe$_2$O$_3$@g-C$_3$N$_4$ Composite with Excellent Visible Light Photocatalytic Activity

**Huoli Zhang [1], Changxin Zhu [1], Jianliang Cao [1,\*], Qingjie Tang [1], Man Li [1], Peng Kang [2], Changliang Shi [1,\*] and Mingjie Ma [1]**

[1] School of Chemistry and Chemical Engineering, Henan Key Laboratory of Coal Green Conversion, The Collaboration Innovation Center of Coal Safety Production of Henan Province, Henan Polytechnic University, Jiaozuo 454003, China; zhanghuoli@hpu.edu.cn (H.Z.); zhuchangxin6@163.com (C.Z.); tangqj521@163.com (Q.T.); liman941128@163.com (M.L.); mingjie8@163.com (M.M.)

[2] College of Materials Science and Engineering, Beijing University of Chemical Technology, Beijing 100029, China; kangpeng.bjhy@sinopec.com

\* Correspondence: caojianliang@hpu.edu.cn (J.C.); scl303@126.com (C.S.); Tel.: +86-391-398-6952 (J.C. & C.S.)

check for updates

**Abstract:** In this study, $\alpha$-Fe$_2$O$_3$@g-C$_3$N$_4$ photocatalyst was synthesized using an ultrasonic assisted self-assembly preparation method. The $\alpha$-Fe$_2$O$_3$@g-C$_3$N$_4$ photocatalyst had a stronger optical absorption in the visible light region than pure graphitic carbon nitride (g-C$_3$N$_4$). The Z-Scheme heterojunction between $\alpha$-Fe$_2$O$_3$ and g-C$_3$N$_4$ significantly inhibited the recombination of electrons and holes. The photocatalytic performances of $\alpha$-Fe$_2$O$_3$@g-C$_3$N$_4$ photocatalyst were excellent in degradation of Rhodamine B (RhB) under visible light irradiation. The results indicated that 5 wt.% $\alpha$-Fe$_2$O$_3$/g-C$_3$N$_4$ had the optimal photocatalytic activity because two-dimension (2D) $\alpha$-Fe$_2$O$_3$ nanosheets can be well-dispersed on the surface of g-C$_3$N$_4$ layers by ultrasonic assisted treatment. A possible photocatalytic mechanism is also discussed.

**Keywords:** $\alpha$-Fe$_2$O$_3$; two-dimension; g-C$_3$N$_4$; photocatalyst; composite

## 1. Introduction

Developing novel and facile preparations of composite photocatalysts is an effective attempt to satisfy high efficiency application in wastewater treatment through sunlight irradiation [1–3]. Heterojunction can promote fast separation of photoinduced electron–hole pairs, especially for composite photocatalysts. To obtain a visible light responsive photocatalytic material, graphitic carbon nitride (g-C$_3$N$_4$) is an appropriate choice as it has a suitable bandgap (2.7 eV); its heterojunction composites have become a focus for research aiming to decrease the recombination of electrons and holes. The advantage of $\alpha$-Fe$_2$O$_3$/g-C$_3$N$_4$ photocatalyst with the Z-scheme heterojunction is that it can realize high quantum efficiency and significantly restrict the recombination of electrons in the g-C$_3$N$_4$ conduction band (CB) and holes in the $\alpha$-Fe$_2$O$_3$ valence band (VB), while retaining strong reducibility and oxidizability; this differs from results for other photocatalysts reported in the literature, such as g-C$_3$N$_4$/BiVO$_4$ [4], C$_3$N$_4$/Cu$_2$O [5], AgFeO$_2$/g-C$_3$N$_4$ [6], C$_3$N$_4$/graphene oxide heterostructure [7] and Pt/g-C$_3$N$_4$ heterostructure [8]. The preparation of Z-scheme heterojunction has attracted great interest due to its adjusting ability of oxidation and reduction [9–13]. More recently, numerous Z-scheme heterojunction composites have been synthesized successfully, including g-C$_3$N$_4$/Au/C-TiO$_2$ [14], g-C$_3$N$_4$/SnS$_2$ [15], CdS/Co$_9$S$_8$ [16], g-C$_3$N$_4$/MnO$_2$ [17], BiVO$_4$/CdS [18], g-C$_3$N$_4$/ZnO [19], TiO$_2$/CdS [20], WO$_3$/g-C$_3$N$_4$ [21], ZnIn$_2$S$_4$/TiO$_2$ [22] and Bi$_{12}$GeO$_{20}$/g-C$_3$N$_4$ [23].

Hematite ($\alpha$-$Fe_2O_3$) is an n-type semiconductor with a suitable bandgap (2.0–2.2 eV) that is employed as a visible light responsive photocatalytic material. $\alpha$-$Fe_2O_3$ can absorb visible light (absorbance edge ∼600 nm) [24,25]. Therefore, the Z-scheme $\alpha$-$Fe_2O_3$/g-$C_3N_4$ heterojunction exhibits an excellent visible light absorbing ability, which can promote photocatalytic activity of water-splitting and $CO_2$ reduction. It has been demonstrated that the Z-scheme heterostructure between $\alpha$-$Fe_2O_3$ and g-$C_3N_4$ effectively separates electrons in the CB of g-$C_3N_4$ and holes in the VB of $\alpha$-$Fe_2O_3$ [26–28]. However, existing synthesis methods for $\alpha$-$Fe_2O_3$/g-$C_3N_4$ heterojunction are time-consuming and involve a complicated process. For example, 2D $\alpha$-$Fe_2O_3$/g-$C_3N_4$ used for water-splitting was synthesized by high-temperature calcination at 550 °C twice [26]. 2D/2D $Fe_2O_3$/g-$C_3N_4$ used for $H_2$ generation was synthesized by rotary evaporation, washing and drying at 80 °C overnight [27]. $\alpha$-$Fe_2O_3$/g-$C_3N_4$ used for $CO_2$ reduction was synthesized by stirring for 24 h to obtain a homogeneous suspension and using the hydrothermal method at 150 °C for 4 h [28].

Herein, $\alpha$-$Fe_2O_3$@g-$C_3N_4$ photocatalyst was synthesized using a simple ultrasonic assisted self-assembly preparation method. Due to the unique hexagonal 2D $\alpha$-$Fe_2O_3$ nanostructure, 2D $\alpha$-$Fe_2O_3$ nanosheets can be dispersed on the surface of g-$C_3N_4$ layers to fabricate the Z-scheme heterojunction. Therefore, the representative 5 wt.% $\alpha$-$Fe_2O_3$@g-$C_3N_4$ composite exhibited excellent catalytic activity for Rhodamine B (RhB) photodegradation, which also had good recycling stability.

## 2. Results and Discussion

### 2.1. Catalyst Characterization

As seen in Figure 1, it can be noticed that all the peaks of pure 2D $\alpha$-$Fe_2O_3$ nanosheets showed the typical characteristic diffraction peaks of $\alpha$-$Fe_2O_3$ phase, which are at 24.1°, 33.1°, 35.6°, 40.9°, 49.5°, 54.1°, 62.5° and 63.9° (JCPDS No.33-0664) [29,30]. For the pure 2D g-$C_3N_4$, two diffraction peaks appearing at 13.2° and 27.8° were observed, which can be attributed to the (100) and (002) diffraction planes respectively (JCPDS No. 87-1526). For 5 wt.% $\alpha$-$Fe_2O_3$@g-$C_3N_4$ photocatalyst, the characteristic peaks belonging to g-$C_3N_4$ (at 13.2° and 27.8°) were detected. Meanwhile, the remaining obvious peaks belonged to $\alpha$-$Fe_2O_3$ phase characteristic diffraction peaks, which were also detected. This indicated that $\alpha$-$Fe_2O_3$ and g-$C_3N_4$ were combined together, implying the formation of $\alpha$-$Fe_2O_3$@g-$C_3N_4$ composite photocatalyst.
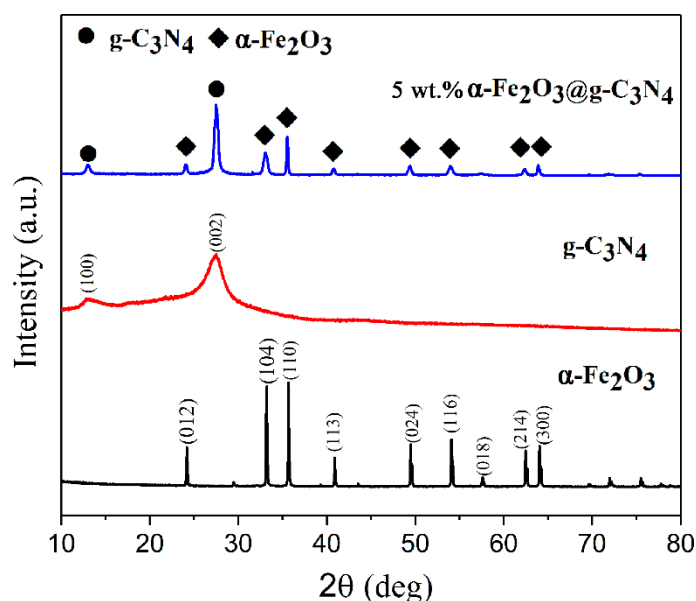


**Figure 1.** XRD patterns of different samples.

The microstructures and morphologies of the samples were observed by scanning electron microscopy (SEM). As seen in Figure 2a,b, the as-obtained $\alpha$-Fe$_2$O$_3$ and g-C$_3$N$_4$ materials were both 2D nanosheet structure; the 2D $\alpha$-Fe$_2$O$_3$ nanosheets were uniform in size. The 2D g-C$_3$N$_4$ were wrinkled due to accumulation and aggregation of g-C$_3$N$_4$ layers. As seen in Figure 2c, 2D $\alpha$-Fe$_2$O$_3$ nanosheets can be well-dispersed on the surface of g-C$_3$N$_4$ layers without obvious agglomeration. The size of the hexagonal 2D $\alpha$-Fe$_2$O$_3$ nanosheets is about 100–150 nm. This shows that the heterojunction can be effectively formed for the representative 5 wt.% $\alpha$-Fe$_2$O$_3$@g-C$_3$N$_4$ photocatalyst. The obtained heterostructure interfaces are beneficial to accelerate the separation of photogenerated electrons and holes during the photocatalytic reaction process. From energy dispersive spectrometry (EDS) of 5 wt.% $\alpha$-Fe$_2$O$_3$@g-C$_3$N$_4$ photocatalyst, the elements of C, N, O and Fe were all detected, as seen in Figure 2d. The coexistence of C, N, O and Fe also indicated the $\alpha$-Fe$_2$O$_3$@g-C$_3$N$_4$ composite formation. Furthermore, the numerous Z-scheme heterojunction interfaces across $\alpha$-Fe$_2$O$_3$ and g-C$_3$N$_4$ can effectively improve charge separation efficiency of $\alpha$-Fe$_2$O$_3$@g-C$_3$N$_4$ photocatalyst [26–28].
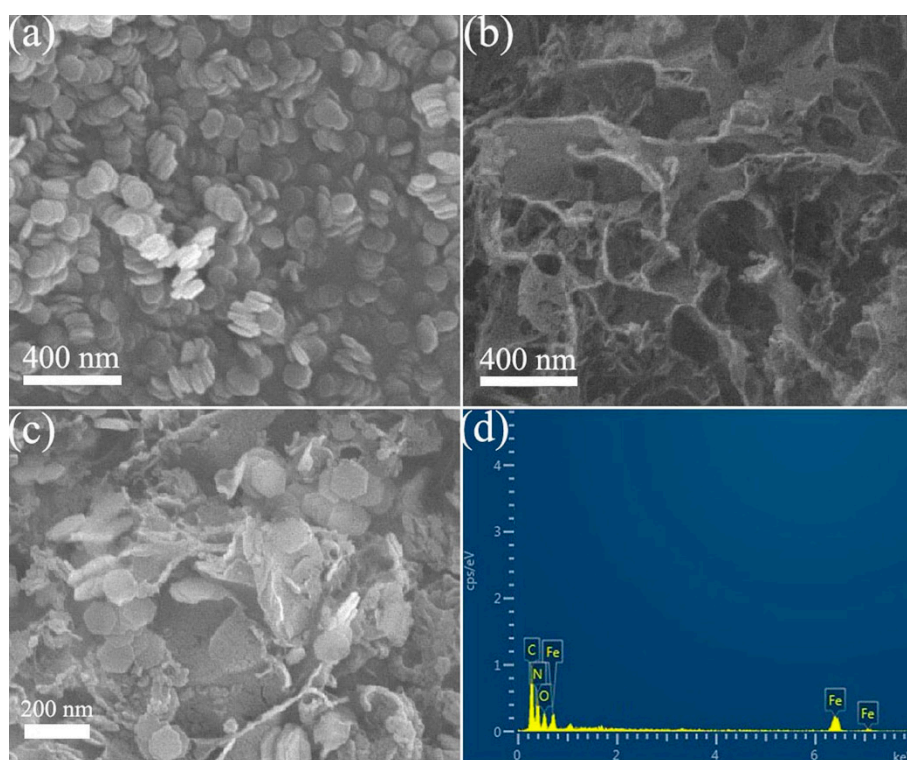


**Figure 2.** SEM images of different samples: (**a**) 2D $\alpha$-Fe$_2$O$_3$, (**b**) 2D g-C$_3$N$_4$, (**c**) 5 wt.% $\alpha$-Fe$_2$O$_3$@g-C$_3$N$_4$ photocatalyst and (**d**) EDS of 5 wt.% $\alpha$-Fe$_2$O$_3$@g-C$_3$N$_4$ photocatalyst.

In order to investigate optical harvest property, the light absorption of the samples was analyzed in the range of 400–750 nm. As seen in Figure 3a, the absorption edge of pure g-C$_3$N$_4$ is at about 460 nm. By comparison, the 5 wt.% $\alpha$-Fe$_2$O$_3$@g-C$_3$N$_4$ composite exhibited obvious redshift, which might be the strong interface interaction of $\alpha$-Fe$_2$O$_3$ and g-C$_3$N$_4$ leading to redshift. Therefore, the representative 5 wt.% $\alpha$-Fe$_2$O$_3$/g-C$_3$N$_4$ photocatalyst shows a stronger visible light harvest ability than 2D g-C$_3$N$_4$. The bandgaps of 2D g-C$_3$N$_4$ and 5 wt.% $\alpha$-Fe$_2$O$_3$@g-C$_3$N$_4$ photocatalyst were analyzed from the intercept of the tangents to the plots of the $(a h \nu)^{1/2}$ versus photon energy. The bandgap was also analyzed through the intercept of the tangents to the plots of the $(a h \nu)^2$ versus photon energy for 2D $\alpha$-Fe$_2$O$_3$. The results show that the bandgaps of 2D g-C$_3$N$_4$, 5 wt.% $\alpha$-Fe$_2$O$_3$@g-C$_3$N$_4$ and 2D $\alpha$-Fe$_2$O$_3$ are 2.71 eV, 2.32 eV and 2.10 eV respectively, as seen in Figure 3b. This revealed that 2D $\alpha$-Fe$_2$O$_3$ nanosheets can effectively broaden the visible light response of the $\alpha$-Fe$_2$O$_3$@g-C$_3$N$_4$ photocatalyst.

The enhanced photoabsorption ability of the $\alpha$-Fe$_2$O$_3$@g-C$_3$N$_4$ photocatalyst will moderately improve the photocatalytic performance.
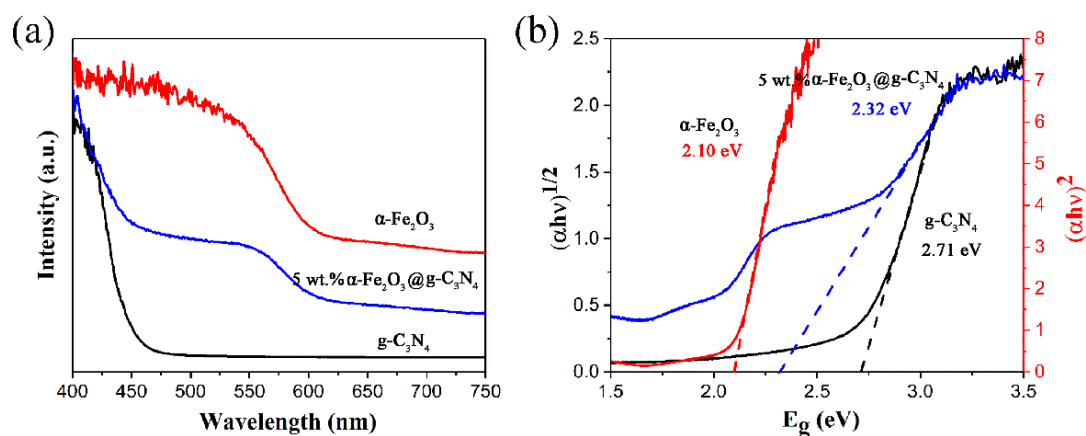


**Figure 3.** (**a**) UV-vis diffuse reflectance spectra (UV–vis DRS) of different samples, (**b**) plots of the $(ah\nu)^{1/2}$ versus photon energy (hv) for g-C$_3$N$_4$ and 5 wt.% $\alpha$-Fe$_2$O$_3$@g-C$_3$N$_4$ photocatalyst; plots of the $(ah\nu)^2$ versus photon energy (hv) for $\alpha$-Fe$_2$O$_3$.

## 2.2. Catalytic Performance

The photocatalytic performances were investigated through photodegradation RhB reaction under visible light irradiation. The results indicate that the photodegradation percentages of $\alpha$-Fe$_2$O$_3$, g-C$_3$N$_4$, 5 wt.% $\alpha$-Fe$_2$O$_3$@g-C$_3$N$_4$ photocatalyst, 10 wt.% $\alpha$-Fe$_2$O$_3$@g-C$_3$N$_4$ photocatalyst and 20 wt.% $\alpha$-Fe$_2$O$_3$@g-C$_3$N$_4$ photocatalyst are 20%, 26%, 90%, 75% and 60% after 120 min, respectively. In addition, in order to demonstrate the visible light photocatalytic system, Evonik P-25 was used in the photocatalytic system under the same conditions. The result showed that P-25 had no photocatalytic activity, which indicates that the photodegradation RhB system is the visible light photocatalytic system, as seen in Figure 4A. As seen in Figure 4B, there was a linear relationship of photodegradation RhB between $\ln(C_0/C)$ and reaction time, which is well followed the first-order kinetics according to the regression factors ($R^2$). As seen in Figure 4C, the values of rate constant k are 0.0024 min$^{-1}$, 0.0179 min$^{-1}$, 0.0111 min$^{-1}$ and 0.0080 min$^{-1}$ for g-C$_3$N$_4$, 5 wt.% $\alpha$-Fe$_2$O$_3$@g-C$_3$N$_4$ photocatalyst, 10 wt.% $\alpha$-Fe$_2$O$_3$@g-C$_3$N$_4$ photocatalyst and 20 wt.% $\alpha$-Fe$_2$O$_3$@g-C$_3$N$_4$ photocatalyst respectively. The rate constant k value of 5 wt.% $\alpha$-Fe$_2$O$_3$@g-C$_3$N$_4$ photocatalyst is nearly 7.4 times larger than the pure 2D g-C$_3$N$_4$. As seen in Figure 4D, 5 wt.% $\alpha$-Fe$_2$O$_3$@g-C$_3$N$_4$ photocatalyst showed the optimal photocatalytic activity, which was used for the recycling test. The results showed that 5 wt.% $\alpha$-Fe$_2$O$_3$@g-C$_3$N$_4$ photocatalyst still had a good stability after four cycles. In addition, as the amount of 2D $\alpha$-Fe$_2$O$_3$ nanosheets increased in the $\alpha$-Fe$_2$O$_3$@g-C$_3$N$_4$ photocatalyst, the rate constant k values of the $\alpha$-Fe$_2$O$_3$@g-C$_3$N$_4$ photocatalyst were gradually decreased. This can be attributed to the agglomeration of 2D $\alpha$-Fe$_2$O$_3$ nanosheets on the surface of g-C$_3$N$_4$. As seen in Figure 5, for 10 wt.% $\alpha$-Fe$_2$O$_3$@g-C$_3$N$_4$ photocatalyst and 20 wt.% $\alpha$-Fe$_2$O$_3$@g-C$_3$N$_4$ photocatalyst, excessive agglomeration of 2D $\alpha$-Fe$_2$O$_3$ nanosheets was observed.
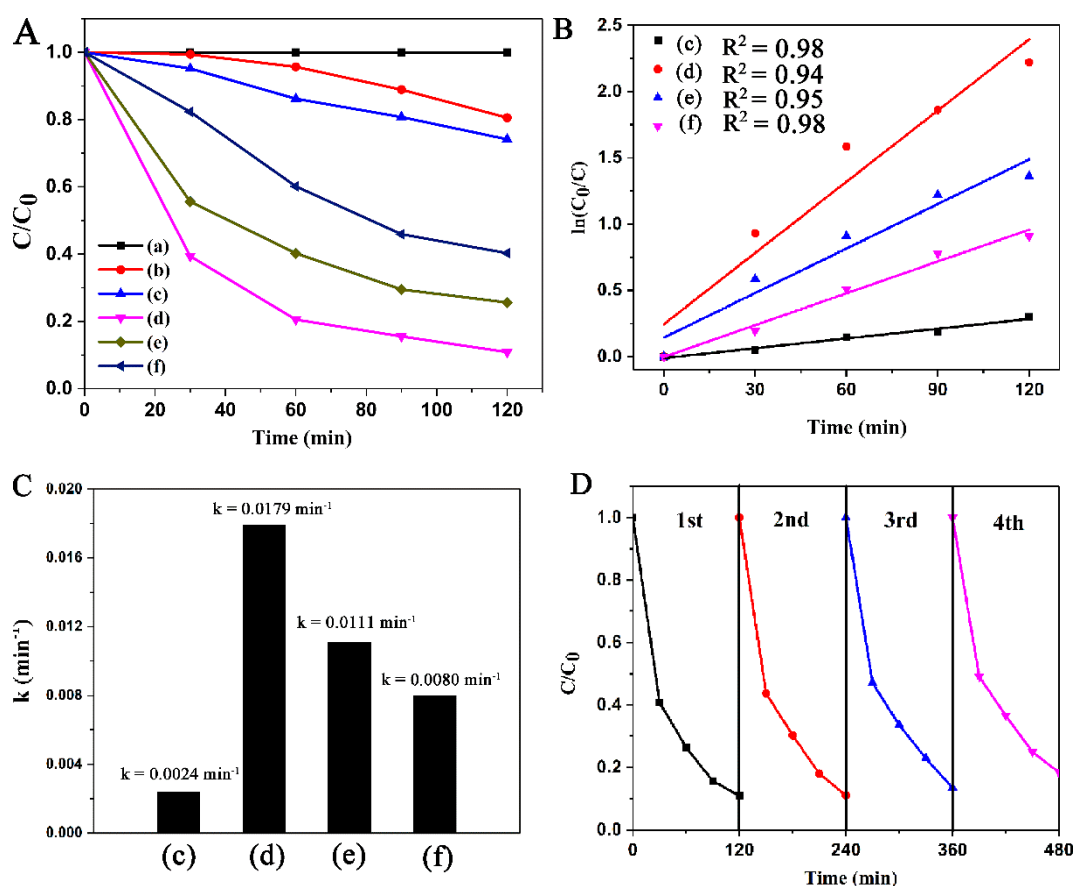
**Figure 4.** (**A**) Photocatalytic performances of different samples, (**B**) kinetic curves of the as-prepared samples, (**C**) rate constant k of the samples: (a) P-25, (b) $\alpha$-Fe$_2$O$_3$, (c) g-C$_3$N$_4$, (d) 5 wt.% $\alpha$-Fe$_2$O$_3$@g-C$_3$N$_4$ photocatalyst, (e) 10 wt.% $\alpha$-Fe$_2$O$_3$@g-C$_3$N$_4$ photocatalyst, (f) 20 wt.% $\alpha$-Fe$_2$O$_3$@g-C$_3$N$_4$ photocatalyst and (**D**) recycling runs of 5 wt.% $\alpha$-Fe$_2$O$_3$@g-C$_3$N$_4$ photocatalyst.
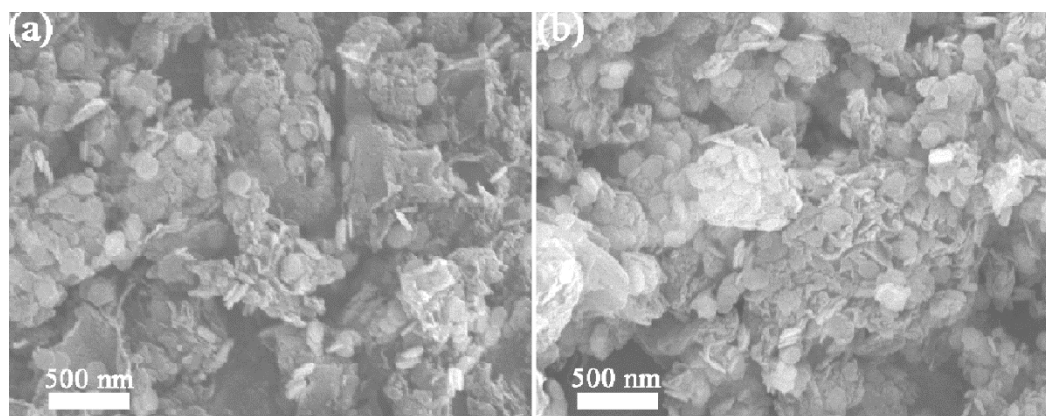


**Figure 5.** SEM images of (**a**) 10 wt.% $\alpha$-Fe$_2$O$_3$@g-C$_3$N$_4$ photocatalyst and (**b**) 20 wt.% $\alpha$-Fe$_2$O$_3$@g-C$_3$N$_4$ photocatalyst.

## 2.3. Photocatalytic Mechanism

For the enhanced photocatalytic activity of $\alpha$-Fe$_2$O$_3$@g-C$_3$N$_4$ photocatalyst, the charge carrier separation and transfer are discussed, as seen in Figure 6. A reasonable photocatalystic mechanism can be described as follows:
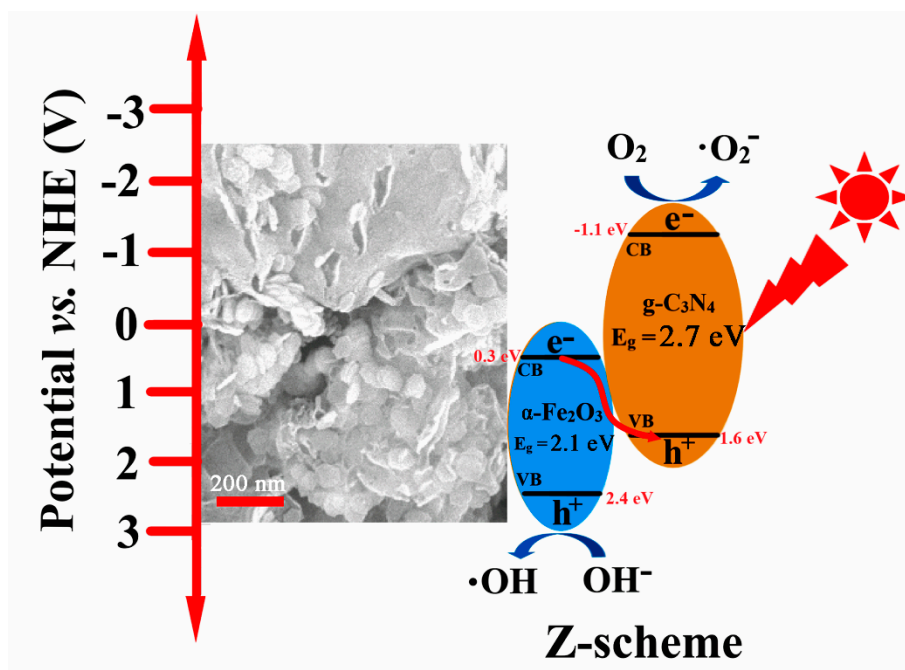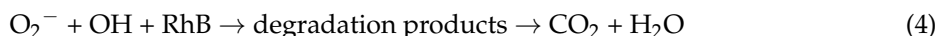
$$\alpha\text{-Fe}_2\text{O}_3@\text{g-C}_3\text{N}_4 + \text{visible light} \rightarrow e^- + h^+ \tag{1}$$

$$e^- + O_2 \rightarrow O_2{}^- \tag{2}$$

$$h^+ + H_2O \rightarrow OH + H^+ \tag{3}$$

$$O_2{}^- + OH + RhB \rightarrow \text{degradation products} \rightarrow CO_2 + H_2O \tag{4}$$
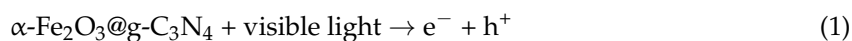


**Figure 6.** Schematic illustration of the charge carrier separation and transfer on $\alpha$-Fe$_2$O$_3$@g-C$_3$N$_4$ photocatalyst.

Both $\alpha$-Fe$_2$O$_3$ and g-C$_3$N$_4$ can be excited under visible light irradiation. Photoinduced holes and electrons can be obtained in their VB and CB, respectively. The CB location of g-C$_3$N$_4$ ($-1.1$ eV vs. normal hydrogen electrode (NHE)) is more negative than that of $\alpha$-Fe$_2$O$_3$ (0.3 eV vs. NHE), and the VB location of $\alpha$-Fe$_2$O$_3$ (2.4 eV vs. NHE) is more positive than that of g-C$_3$N$_4$ (1.6 eV vs. NHE) [31,32]. Through Z-scheme heterojunction, the photoinduced electrons in the CB location of $\alpha$-Fe$_2$O$_3$ can migrate to the VB location of g-C$_3$N$_4$ and further combine with photogenerated holes in the VB location of g-C$_3$N$_4$. The charge migration follows the Z-scheme route, which can effectively inhibit the recombination of the photogenerated electrons in the CB location of g-C$_3$N$_4$. The photogenerated holes and electrons respectively accumulate in the VB location of $\alpha$-Fe$_2$O$_3$ and the CB location of g-C$_3$N$_4$, keeping the strong oxidizability and reducibility [27,28]. Significantly, the Z-scheme heterojunction not only enhances visible light absorption ability, but also improves charge separation efficiency, leading to a notable enhancement for photocatalytic activity of $\alpha$-Fe$_2$O$_3$@g-C$_3$N$_4$ photocatalyst.

## 3. Materials and Methods

### 3.1. Synthesis

The chemical reagents in this study were of analytical grade. Deionized water was used in this work. The nanosheets of 2D g-C$_3$N$_4$ and hexagonal 2D $\alpha$-Fe$_2$O$_3$ were synthesized according to previously reported methods [33–35]. In a typical synthesis, the 2D $\alpha$-Fe$_2$O$_3$@g-C$_3$N$_4$ photocatalyst was prepared using an ultrasonic assisted self-assembly method. First, 95 mg of 2D g-C$_3$N$_4$ was added into 10 mL ethanol by stirring in an ultrasonic bath. Subsequently, 5 mg of 2D $\alpha$-Fe$_2$O$_3$ nanosheets and 50 μL of Nafion solution (5 wt.% Nafion, Sigm$\alpha$-Aldrich, DuPont, Wilmington, DE, USA), as stabilizing agents, were added to the mixture in that order. The mixture was irradiated under

the 40 kHz ultrasonic wave with power output of 240 W for 30 min. The as-obtained suspension was dried at 80 °C for 12 h. The dried product was collected. In order to remove stabilizing agent, the product was washed several times with ethanol and deionized water. Then the product was dried at 60 °C for 12 h. Finally, the as-obtained 5 wt.% $\alpha$-Fe$_2$O$_3$@g-C$_3$N$_4$ composite was obtained used as visible light photocatalyst. Different amounts of $\alpha$-Fe$_2$O$_3$ were used for preparing 10 wt.% and 20 wt.% $\alpha$-Fe$_2$O$_3$@g-C$_3$N$_4$ photocatalyst under the same preparation conditions. The schematic illustration is shown in Figure 7. The 2D $\alpha$-Fe$_2$O$_3$@g-C$_3$N$_4$ photocatalyst can be synthesized though the ultrasonic assisted self-assembly route.
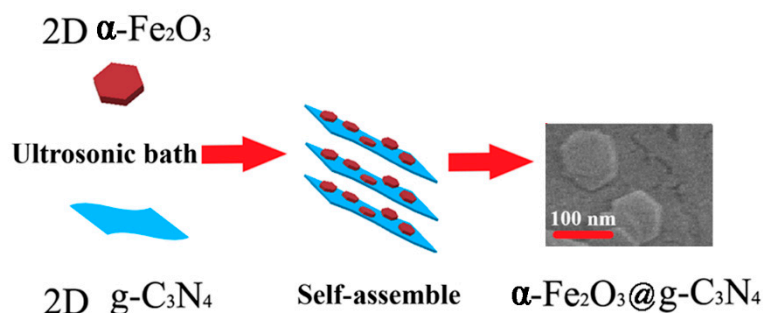


**Figure 7.** Schematic illustration for the 2D $\alpha$-Fe$_2$O$_3$@g-C$_3$N$_4$ photocatalyst synthesis.

*3.2. Characterizations*

Scanning electron microscopy (SEM) was used to observe morphology of different samples using FEI (Quanta 250 FEG, Eindhoven, The Netherlands) microscopy. The energy dispersive spectrometry (EDS) was analyzed by X-Max (Oxford Instruments, Oxford, UK). The X-ray powder diffraction (XRD) patterns were recorded by AXSD8 (Bruker, Madison, WI, USA) with CuK$\alpha$ as a radiation source. The operating voltage and current were at 40 kV and 40 mA, respectively. The UV-vis diffuse reflectance spectra (UV-vis DRS) was investigated by using UV-240 (Shimadzu, Kyoto, Japan).

*3.3. Photocatalytic Tests*

2D $\alpha$-Fe$_2$O$_3$@g-C$_3$N$_4$ photocatalyst was used for photodegradation RhB to evaluate the photocatalytic activity. The photocatalytic tests were performed at visible light irradiation of a halogen lamp (Osram, Munich, Germany, 220 V and 500 W) with a UV-cutoff filter (Shanghai Seagull Colored Optical Glass Co., Ltd., Shanghai, China) ($\lambda > 420$ nm). First, 100 mg as-prepared sample was added in 100 mL RhB (10 mg/L). Subsequently, the as-obtained solution was kept in the dark and stirred for 30 min to ensure an adsorption and desorption equilibrium. After this, the mixture solution at 10 cm from the halogen lamp was irradiated under visible light. Additionally, a certain amount of the mixture solution was pipetted and centrifuged every 30 min until 120 min. The RhB concentration of the centrifuged aqueous solution was measured by UV–vis spectrophotometer using TU1900 (Beijing purkinje general instrument Co., Ltd., Beijing, China).

**4. Conclusions**

In summary, 2D $\alpha$-Fe$_2$O$_3$@g-C$_3$N$_4$ photocatalyst was successfully synthesized using a simple ultrasonic assisted self-assembly preparation method. The results indicate that 2D $\alpha$-Fe$_2$O$_3$ were dispersed on the surface of g-C$_3$N$_4$. The 2D $\alpha$-Fe$_2$O$_3$@g-C$_3$N$_4$ photocatalyst is very suitable to obtain Z-scheme heterojunction as charge transfer route. The 5 wt.% $\alpha$-Fe$_2$O$_3$@g-C$_3$N$_4$ photocatalyst showed excellent catalytic activity and a good recycling stability for photodegradation RhB under visible light irradiation. The $\alpha$-Fe$_2$O$_3$@g-C$_3$N$_4$ photocatalyst, synthesized using a simple ultrasonic assisted self-assembly method, obtained an improvement of visible light photocatalytic activity, providing a route to synthesize g-C$_3$N$_4$-based photocatalysts.

## References

1.　Low, J.; Jiang, C.; Cheng, B.; Wageh, S.; AI-Ghamdi, A.A.; Yu, J. A review of direct Z-Scheme photocatalysts. *Small Methods* **2017**, *1*, 1700080. [CrossRef]

2.　Li, X.; Yu, J.; Jaroniec, M. Hierarchical photocatalysts. *Chem. Soc. Rev.* **2016**, *45*, 2603–2636. [CrossRef] [PubMed]

3.　Low, J.; Yu, J.; Jaroniec, M.; Wageh, S.; AI-Ghamdi, A.A. Heterojunction photocatalysts. *Adv. Mater.* **2017**, *29*. [CrossRef] [PubMed]

4.　Cheng, J.; Yan, X.; Mo, Q.; Liu, B.; Wang, J.; Yang, X.; Li, L. Facile synthesis of g-$C_3N_4$/$BiVO_4$ heterojunctions with enhanced visible light photocatalytic performance. *Ceram. Int.* **2017**, *43*, 301–307. [CrossRef]

5.　Tian, Y.; Chang, B.; Fu, J.; Zhou, B.; Liu, J.; Xi, F.; Dong, X. Graphitic carbon nitride/$Cu_2O$ heterojunctions: Preparation, characterization, and enhanced photocatalytic activity under visible light. *J. Solid State Chem.* **2014**, *212*, 1–6. [CrossRef]

6.　Tang, D.; Zhang, G. Fabrication of $AgFeO_2$/g-$C_3N_4$ nanocatalyst with enhanced and stable photocatalytic performance. *Appl. Surf. Sci.* **2017**, *391*, 415–422. [CrossRef]

7.　Wan, W.; Yu, S.; Dong, F.; Zhang, Q.; Zhou, Y. Efficient $C_3N_4$/graphene oxide macroscopic aerogel visible-light photocatalyst. *J. Mater. Chem. A* **2016**, *4*, 7823–7829. [CrossRef]

8.　Fina, F.; Ménard, H.; Irvine, J.T.S. The effect of Pt NPs crystallinity and distribution on the photocatalytic activity of Pt-g-$C_3N_4$. *Phys. Chem. Chem. Phys.* **2015**, *17*, 13929–13936. [CrossRef] [PubMed]

9.　Wang, Q.; Hisatomi, T.; Jia, Q.X.; Tokudome, H.; Zhong, M.; Wang, C.Z.; Pan, Z.; Takata, T.; Nakabayashi, M.; Shibata, N.; et al. Scalable water splitting on particulate photocatalyst sheets with a solar-to-hydrogen energy conversion efficiency exceeding 1%. *Nat. Mater.* **2016**, *15*, 611–615. [CrossRef] [PubMed]

10.　Chen, S.S.; Qi, Y.; Hisatomi, T.; Ding, Q.; Asai, T.; Li, Z.; Ma, S.S.K.; Zhang, F.; Domen, K.; Li, C. Efficient visible-light-driven Z-Scheme overall water splitting using a $MgTa_2O_{6-x}N_y$/TaON heterostructure photocatalyst for $H_2$ evolution. *Angew. Chem. Int. Ed.* **2015**, *127*, 8618–8621. [CrossRef]

11.　Wu, X.; Zhao, J.; Wang, L.; Han, M.; Zhang, M.; Wang, H.; Huang, H.; Liu, Y.; Kang, Z. Carbon dots as solid-state electron mediator for $BiVO_4$/CDs/CdS Z-scheme photocatalyst working under visible light. *Appl. Catal. B Environ.* **2017**, *206*, 501–509. [CrossRef]

12.　Ou, M.; Wan, S.; Zhong, Q.; Zhang, S.; Song, Y.; Guo, L.; Cai, W.; Xu, Y. Hierarchical Z-scheme photocatalyst of g-$C_3N_4$@Ag/$BiVO_4$ (040) with enhanced visible-light-induced photocatalytic oxidation performance. *Appl. Catal. B Environ.* **2018**, *221*, 97–107. [CrossRef]

13.　Ng, B.J.; Putri, L.K.; Tan, L.L.; Pasbakhsh, P.; Chai, S.P. All-solid-state Z-scheme photocatalyst with carbon nanotubes as an electron mediator for hydrogen evolution under simulated solar light. *Chem. Eng. J.* **2017**, *316*, 41–49. [CrossRef]

14.　Zou, Y.; Shi, J.W.; Ma, D.; Fan, Z.; Niu, C.; Wang, L. Fabrication of g-$C_3N_4$/Au/C-$TiO_2$ hollow structures as visible-light-driven Z-scheme photocatalysts with enhanced photocatalytic $H_2$ evolution. *ChemCatChem* **2017**, *9*, 3752–3761. [CrossRef]

15.　Di, T.; Zhu, B.; Cheng, B.; Yu, J.; Xu, J. A direct Z-scheme g-$C_3N_4$/$SnS_2$ photocatalyst with superior visible-light $CO_2$ reduction performance. *J. Catal.* **2017**, *352*, 532–541. [CrossRef]

16.　Qiu, B.; Zhu, Q.; Du, M.; Fan, L.; Xing, M.; Zhang, J. Efficient solar light harvesting CdS/$Co_9S_8$ hollow cubes for Z-scheme photocatalytic water splitting. *Angew. Chem. Int. Ed.* **2017**, *129*, 2728–2732. [CrossRef]

17.　Xia, P.; Zhu, B.; Cheng, B.; Yu, J.; Xu, J. 2D/2D g-$C_3N_4$/$MnO_2$ nanocomposite as a direct Z-scheme photocatalyst for enhanced photocatalytic activity. *ACS Sustain. Chem. Eng.* **2017**, *6*, 965–973. [CrossRef]

18. Zhou, F.Q.; Fan, J.C.; Xu, Q.J.; Min, Y.L. BiVO$_4$ nanowires decorated with CdS nanoparticles as Z-scheme photocatalyst with enhanced H$_2$ generation. *Appl. Catal. B Environ.* **2017**, *201*, 77–83. [CrossRef]

19. Wang, J.; Xia, Y.; Zhao, H.; Wang, G.; Xaing, L.; Xu, J.; Komarneni, S. Oxygen defects-mediated Z-scheme charge separation in g-C$_3$N$_4$/ZnO photocatalysts for enhanced visible-light degradation of 4-chlorophenol and hydrogen evolution. *Appl. Catal. B Environ.* **2017**, *206*, 406–416. [CrossRef]

20. Meng, A.; Zhu, B.; Zhong, B.; Zhang, L.; Cheng, B. Direct Z-scheme TiO$_2$/CdS hierarchical photocatalyst for enhanced photocatalytic H$_2$-production activity. *Appl. Surf. Sci.* **2017**, *422*, 518–527. [CrossRef]

21. Cui, L.; Ding, X.; Wang, Y.; Shi, H.; Huang, L.; Zuo, Y.; Kang, S. Facile preparation of Z-scheme WO$_3$/g-C$_3$N$_4$ composite photocatalyst with enhanced photocatalytic performance under visible light. *Appl. Surf. Sci.* **2017**, *391*, 202–210. [CrossRef]

22. Yang, G.; Chen, D.; Ding, H.; Feng, J.; Zhang, J.Z.; Zhu, Y.; Hamid, S.; Bahnemann, D.W. Well-designed 3D ZnIn$_2$S$_4$ nanosheets/TiO$_2$ nanobelts as direct Z-scheme photocatalysts for CO$_2$ photoreduction into renewable hydrocarbon fuel with high efficiency. *Appl. Catal. B Environ.* **2017**, *219*, 611–618. [CrossRef]

23. Wan, Z.; Zhang, G.; Wu, X.; Yin, S. Novel visible-light-driven Z-scheme Bi$_{12}$GeO$_{20}$/g-C$_3$N$_4$ photocatalyst: Oxygen-induced pathway of organic pollutants degradation and proton assisted electron transfer mechanism of Cr (VI) reduction. *Appl. Catal. B Environ.* **2017**, *207*, 17–26. [CrossRef]

24. Mishra, M.; Chun, D.M. α-Fe$_2$O$_3$ as a photocatalytic material: A review. *Appl. Catal. A Gen.* **2015**, *498*, 126–141. [CrossRef]

25. Wheeler, D.A.; Wang, G.; Ling, Y.; Li, Y.; Zhang, J.Z. Nanostructured hematite: Synthesis, characterization, charge carrier dynamics, and photoelectrochemical properties. *Energy Environ. Sci.* **2012**, *5*, 6682–6702. [CrossRef]

26. She, X.; Wu, J.; Xu, H.; Zhong, J.; Wang, Y.; Song, Y.; Nie, K.; Liu, Y.; Yang, Y.; Rodrigues, M.T.F.; et al. High efficiency photocatalytic water splitting using 2D α-Fe$_2$O$_3$/g-C$_3$N$_4$ Z-Scheme Catalysts. *Adv. Energy Mater.* **2017**, *7*, 1700025. [CrossRef]

27. Xu, Q.; Zhu, B.; Jiang, C.; Cheng, B.; Yu, J. Constructing 2D/2D Fe$_2$O$_3$/g-C$_3$N$_4$ direct Z-scheme photocatalysts with enhanced H$_2$ generation performance. *Sol. RRL* **2018**, *2*, 1800006. [CrossRef]

28. Jiang, Z.; Wan, W.; Li, H.; Yuan, S.; Zhao, H.; Wong, P.K. A hierarchical Z-scheme α-Fe$_2$O$_3$/g-C$_3$N$_4$ hybrid for enhanced photocatalytic CO$_2$ reduction. *Adv. Mater.* **2018**, *30*, 1706108. [CrossRef] [PubMed]

29. Xie, J.; Zhang, L.; Li, M.; Hao, Y.; Lian, Y.; Li, Z.; Wei, Y. α-Fe$_2$O$_3$ modified ZnO flower-like microstructures with enhanced photocatalytic performance for pentachlorophenol degradation. *Ceram. Int.* **2015**, *41*, 9420–9425. [CrossRef]

30. Xie, J.; Zhou, Z.; Lian, Y.; Hao, Y.; Li, P.; Wei, Y. Synthesis of α-Fe$_2$O$_3$/ZnO composites for photocatalytic degradation of pentachlorophenol under UV–vis light irradiation. *Ceram. Int.* **2015**, *41*, 2622–2625. [CrossRef]

31. Cao, S.; Low, J.; Yu, J.; Jaroniec, M. Polymeric photocatalysts based on graphitic carbon nitride. *Adv. Mater.* **2015**, *27*, 2150–2176. [CrossRef] [PubMed]

32. Wang, J.C.; Zhang, L.; Fang, W.X.; Ren, J.; Li, Y.Y.; Yao, H.C.; Wang, J.S.; Li, Z.J. Enhanced photoreduction CO$_2$ activity over direct Z-scheme α-Fe$_2$O$_3$/Cu$_2$O heterostructures under visible light irradiation. *ACS Appl. Mater. Interfaces* **2015**, *7*, 8631–8639. [CrossRef] [PubMed]

33. Chen, L.; Yang, X.; Chen, J.; Liu, J.; Wu, H.; Zhan, H.; Liang, C.; Wu, M. Continuous shape-and spectroscopy-tuning of hematite nanocrystals. *Inorg. Chem.* **2010**, *49*, 8411–8420. [CrossRef] [PubMed]

34. Gong, Y.; Wang, Y.; Sun, G.; Jia, T.; Jia, L.; Zhang, F.; Lin, L.; Zhang, B.; Cao, J.; Zhang, Z. Carbon nitride decorated ball-flower like Co$_3$O$_4$ hybrid composite: Hydrothermal synthesis and ethanol gas sensing application. *Nanomaterials* **2018**, *8*, 132. [CrossRef] [PubMed]

35. Cao, J.; Gong, Y.; Wang, Y.; Zhang, B.; Zhang, H.; Sun, G.; Bala, H.; Zhang, Z. Cocoon-like ZnO decorated graphitic carbon nitride nanocomposite: Hydrothermal synthesis and ethanol gas sensing application. *Mater. Lett.* **2017**, *198*, 76–80. [CrossRef]